

MONTHLY WEATHER REVIEW

VOLUME 93, NUMBER 9

SEPTEMBER 1965

TIROS III RADIATION MEASUREMENTS AND SOME DIABATIC PROPERTIES OF THE ATMOSPHERE*

PAUL A. DAVIS

Stanford Research Institute, Menlo Park, Calif.

ABSTRACT

A basic objective of this study was to evaluate the applicability of medium-resolution satellite radiation measurements to assessments of the diabatic heating and cooling within the atmosphere. Data from portions of TIROS III orbital passes in mid-July 1961 and concurrent conventional data were examined over a 4-by-4-degree grid scale. Computations, appropriate to analyzed cloud conditions for each grid block, included the outgoing long-wave flux, the infrared radiational cooling, the total radiational cooling (including solar absorption in the atmosphere), and the total potential energy. In addition, simple relative estimates were made of the latent heat released and the average boundary heat flux into the atmosphere.

Results show that, for nadir angles less than about 45 deg., the unaltered Channel 2 temperature is proportional to the computed outgoing long-wave flux and is related to the average cloudiness in each grid block. The Channel 2 temperature has a higher positive correlation with the total radiational cooling (long-wave and short-wave) in the atmosphere than with the long-wave cooling alone. The relative heating from the distributions of net radiation and precipitation are correlated in the same sense to the Channel 2 temperature, but the relative boundary heat flux is correlated in the opposite sense. Unaltered Channel 3 fluxes show a general relationship to atmospheric solar absorption rates and to a cloudiness parameter for the grid scale.

Some slight generation of eddy potential energy was suggested by the analyses of the differential diabatic cooling.

1. INTRODUCTION

The satellite system of meteorological observation ultimately will be evaluated in terms of improvements in accounts of the *evolving* state of the atmosphere. Consequently, efforts are made to obtain direct radiometric observations that may provide useful quantitative input to numerical studies of atmospheric circulation. For example, existing satellite radiometers are capable of providing a spectrally-integrated measure of the net incoming or outgoing radiation at the top of the atmosphere. The spatial distribution of this planetary net radiation prescribes the relative heat sources for heat storage or transport (and transformation) in the land-ocean-atmosphere system. In order to describe directly

the differential diabatic heating or cooling within the atmosphere alone, other information is needed.

A basic goal of the present study is to examine the applicability of medium-resolution satellite radiation measurements to specifications of relative diabatic heating and cooling in the atmosphere on a scale of about half the wavelength of the smallest "synoptic" eddies. Large scales (e.g., zonal averages around the hemisphere during a month) are not examined here. With the aid of numerous conventional observations, the procedure is first to describe objectively the cloudiness for each grid block, then to specify the infrared cooling, the solar heating, and at least an indication of the relative distributions of the net release of latent heat and the heat flow across the lower boundary of the atmosphere. Since grid regions are selected on the basis of satellite orbital passes, the estimated diabatic parameters are compared directly with concurrent satellite measurements.

*This research was supported by the Goddard Space Flight Center, National Aeronautics and Space Administration, under contract NAS 5-2919.

2. MEDIUM-RESOLUTION RADIATION DATA FROM TIROS

Numerical studies (cf. Mintz [12]) suggest that the minimum spatial dimension for general analysis need not be smaller than "several hundred kilometers." Although it is possible to utilize low-resolution radiation measurements for this scale, it can be advantageous to analyze medium-resolution measurements. By so doing, the partial contributions from all portions of a grid area can be weighted more uniformly and evaluations of slant-path and background effects can be made more easily. The minimum time scale of prime importance to studies of the global energy balance and circulation need not include periods as short as the diurnal cycle. However, since the TIROS satellites to date have provided radiometric data at a variety of local times within each orbital swath, the spatial distributions of radiometric observations contain "irregularities" of diurnal origin.

All of the satellite data employed in this study were taken from the early orbital passes of TIROS III. The medium-resolution radiometric instrumentation and the earth-scanning modes of TIROS III have been discussed in considerable detail [1], [15], [16]. Principal signal contributions for a direct earth-view (zero nadir angle) came from an area of about 3700 km.² The size of the viewed area increased rapidly as nadir angles were increased beyond 45 deg., becoming about an order of magnitude larger at a 55-deg. nadir angle than at a zero-degree nadir angle. Analyses were confined to data from radiometric nadir angles of about 45 deg. or less.

Figure 1 illustrates a hypothetical response of the TIROS III five-channel radiometer for views of water, land, and cloud, with the land considered to be warmer than the water. Responses of the infrared channels appear on the left side of figure 1 in terms of equivalent blackbody temperature; a single dashed curve represents the responses of both solar channels in watts per square meter. The quantitative interpretation of singular responses or multiple responses from two or more aligned channels is hindered by instrumental uncertainties (especially differential degradation), view-angle dependencies for each channel, inhomogeneities within the field of view, and ambiguities, such as the lack of distinction between a high semitransparent overcast and a lower or less extensive non-transparent cloud cover. Data from Channels 2 and 3 (or 5) reveal the principal relative variations in radiometric response. Most of the change of the infrared emittance from the earth-atmosphere occurs with changing cloud or surface conditions and is confined primarily to the broad spectral region covered by Channel 2. Therefore, little additional information on variations in total emittance is obtained directly from Channel 4. High clouds, which indicate a moist upper troposphere, usually are defined more distinctly in the Channel 2 response than in the response of other channels.

Cloudiness is associated explicitly or implicitly with all

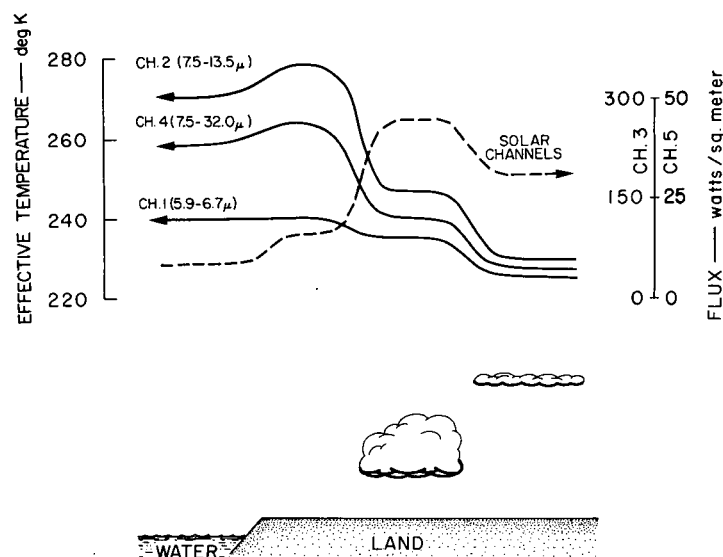


FIGURE 1.—Illustrated response of TIROS III radiometer to terrain and cloud features.

diabatic processes and is directly related to the radiometric response. For an average mid-latitude summertime profile of moisture and temperature and a lower boundary temperature of 292° K., figure 2 illustrates the computed Channel 2 response for directly downward views of opaque surfaces at different altitudes. Although the detailed variations of the temperature moisture structure with cloudiness have not been included, the general pattern of isotherms in figure 2 indicates that distinct cloud-top height information is obtainable from overcast regions, that cloud amount can be described best for high opaque clouds, and that an emission-independent measure of either cloud-top height or cloud amount aids in the description of the other. In the real atmosphere a proportionality often exists between cloud amount and cloud-top height, at least in a statistical sense.

For the analysis of medium-resolution data in middle latitudes, a grid size of 4 deg. of latitude by 4 deg. of longitude was adopted. This grid size is small enough to be associated with a single solar-illumination angle and is compatible with small "synoptic" dimensions in the patterns of radiometric and cloud-cover data. Initial data tabulations over a fixed 2-by-2-deg. array permitted flexibility in the selection of 4-by-4-deg. grid blocks within the area scanned during an arbitrary TIROS orbital pass. Figure 3a illustrates the grids adapted from the 2-by-2 array in order to coincide with a portion of orbital pass 44, TIROS III. The analyzed Channel 2 temperatures were based on averages tabulated over the 2-by-2 array. Figure 3b illustrates the corresponding synoptic data.

3. ATMOSPHERIC HEAT-BALANCE PARAMETERS

The establishment of a relationship between the outgoing infrared flux and the total (radiative and non-radia-

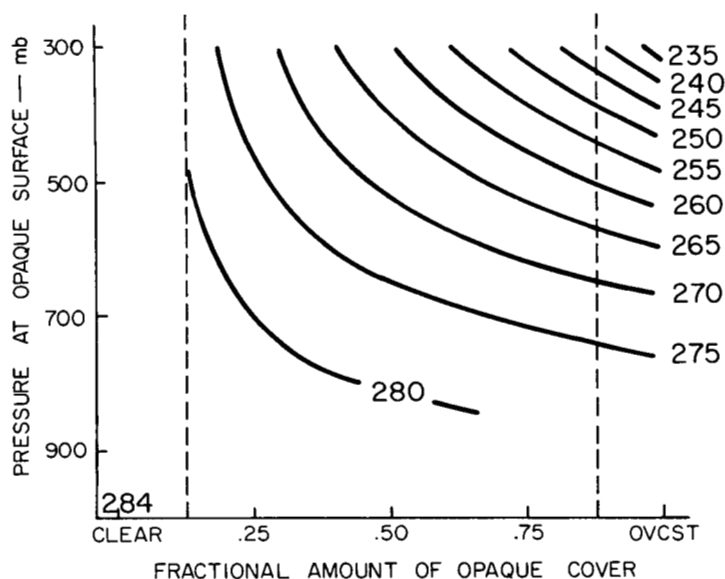
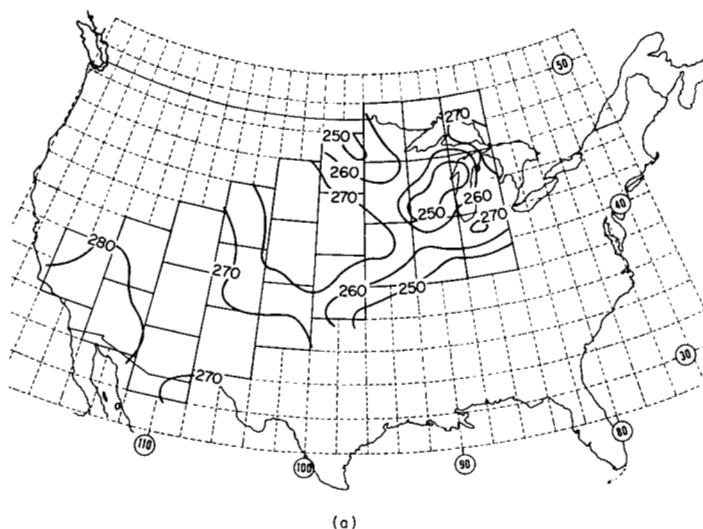


FIGURE 2.—Effective temperatures from Channel 2 versus height and amount of an opaque surface for hypothetical downward view of warm atmosphere.

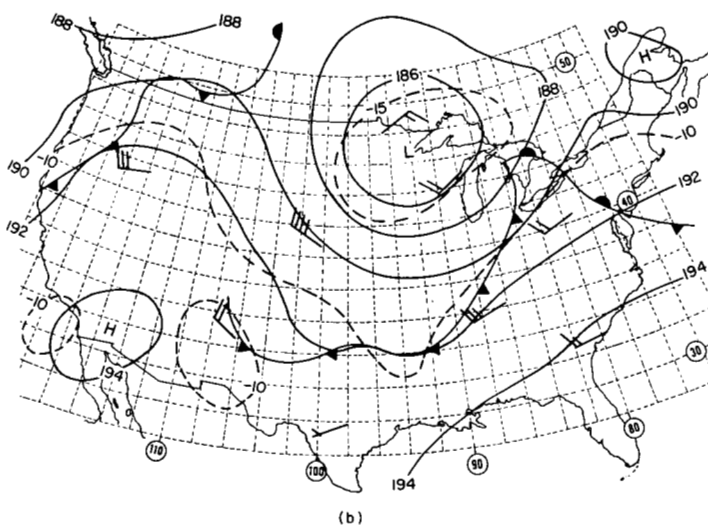
tive) differential diabatic heating on a small synoptic scale is complicated by such factors as horizontal advection, diurnal variations, and the evolution and movement of cloud patterns. Considerable coupling between the outgoing infrared flux (determinable from satellite measurements) and the atmospheric infrared cooling can be anticipated. During cloudy conditions the outgoing flux is primarily related to the cloud-top height, whereas the total cooling is primarily related both to the cloud-top height and to the cloud-base height. Consequently, the correlation between the outgoing flux and the total cooling is variable. During clear skies the relationship between the two parameters is partially governed by the temperature, emissivity, and elevation of the lower boundary.

From local balloon measurements of the net radiation during nocturnal conditions, Sabatini and Suomi [14] and Suomi and Shen [17] have compared statistically the outgoing flux and the total infrared cooling. Without a detailed account of the possible combined effects of clouds, the balloon system, occasional minimal solar illumination, or variations in the lower boundary, their correlation coefficients are large. Clapp's [3, 4] computational studies, which included an examination of other diabatic components and cloudiness, suggest that the outgoing flux is better related to cloudiness than to total infrared cooling, and that diabatic parameters other than the infrared cooling are important to the differential heating, which is the quantity desired.

Discussions of the atmospheric energy cycle and definitions of terminology are given, for example, by Lorenz [11] and Oort [13]. The meridional differential diabatic heating is the prime generator of zonal available potential



(a)



(cf. [2], [10]) have been limited; evaluations of the effects of small-scale synoptic distributions of cloudiness and precipitation are not well documented. Although it may be resolved that the most significant phases of the atmospheric energy cycle are associated with a large scale, the smaller-scale generation processes still may merit identification. For example, even in the presence of an overall destruction of eddy potential energy on a large scale, the sub-scale eddy potential energy generated by some differential diabatic heating conceivably could be transformed to sub-scale eddy kinetic energy that is subsequently transferred to larger scales.

In this limited examination of small sections of the globe with irregular lower boundaries, the eddy energies were not described explicitly. However, between the lower boundary and the height H of an upper-level constant-pressure surface, the total potential energy (i.e., internal plus potential) E was determined for each grid block from:

$$E = z_0(p_0 - p_H) - p_H(z_H - z_0) + c_p g^{-1} \int_{p_H}^{p_0} T dp \quad (1)$$

where z_0 is the surface elevation, p_0 is the surface pressure, p_H is a fixed pressure (100 mb. in this study),

and depth $z_H - z_0$ was determined from $(R/g) \int_{p_H}^{p_0} T d(\ln p)$.

Although the corresponding available potential energy is only a fraction of E , useful comparisons of the grid variations of E can be made with the distribution of diabatic components or vertical motions. The method for specifying the vertical motion over a constant-pressure level within a grid block is outlined briefly in the Appendix.

4. METEOROLOGICAL DATA

The TIROS III data examined include the United States portions of the daytime orbital passes 3 and 4 and the early morning passes 29 and 44. "Conventional" data included upper-air data, hourly surface reports, hourly summary charts of pertinent radar records, and the extensive records of maximum and minimum surface temperatures from regular and cooperative stations. Profiles of temperature and specific humidity were constructed for each grid block from three-dimensional analyses of radiosonde data, but, for the highest levels, climatological data were used.

An objective accounting of cloudiness within each grid block on the basis of conventional data is difficult and laborious. A nephanalysis that is initiated from surface observations can be extended to the regions between reporting stations with the aid of observations of winds, precipitation, and the trends of cloudiness provided by consecutive hourly reports. The distribution of relative humidity, obtained from concurrent radiosonde data, can be used to estimate the cloud boundaries, but for some cirrus only an infinitesimal optical

thickness can be assigned. Satellite television pictures (where available) aid directly in the specification of total cloud amount within each grid block. Available surface observations do not include information on high clouds when the sky is obscured by lower clouds. Furthermore, in regions of sparse data, the continuity of high cloudiness is not readily determined. In these cases the Channel 2 temperatures provide an indication of the extent of existing high clouds. Although computations of the outgoing flux are made without the direct use of Channel 2 temperatures, some bias is introduced in later comparisons of cloudiness and outgoing flux with Channel 2 data over high-cloud distributions. This bias must be tolerated in order to arrive at meaningful comparisons between the satellite measurements and computations of total infrared cooling or solar heating in the atmosphere.

Tabulated results of the nephanalysis for each grid block included the fractional amount of clear skies, the amount and upper boundary of each general cloud type (low, middle, and high) visible from above, the amount and lower boundary of each cloud type visible from below, and, for solar absorption computations, specifications of those areas containing separate but overlapping cloud decks. In addition, a unique non-dimensional classification of the total "cloudiness" within each grid block was made to enable an objective comparison with other parameters. Clouds of each description were weighted by their proportion to the total cloud amount so that a single effective top, bottom, and "bulk" could be assigned to each grid block. The nondimensional cloud classifications are discussed further in Section 6.

Finally, data that described the terrain elevation and surface cover were assembled for the entire grid region. Some modifications were applied to meteorological data obtained from mountain stations with elevations that differed significantly from the terrain elevation in the grid block. The summertime surface cover was classified in six categories: (1) water, (2) forest, (3) forest and grass, (4) moist grassland, (5) semi-arid grazing land or shrubland, and (6) desert. These descriptors, arranged above in terms of increasing albedo and decreasing evapotranspiration, can be used as climatological aids in the estimation of differences in the surface heat flux.

5. ESTIMATES OF DIFFERENTIAL DIABATIC COOLING

Infrared Emission. The techniques that were applied in the computations of the transmission and flux of infrared radiation for spectral intervals beyond $4\frac{1}{2}$ microns have been described in previous reports [5, 7.] In this application the terrain and cloud boundaries were treated as blackbody surfaces. Prime computational emphasis was on the outgoing infrared flux and the total infrared flux divergence (cooling) corresponding to the observed cloud conditions and the average surface temperature. Use of the average surface temperature for the day with the

upper-air conditions at analysis time was designed to suppress the diurnal variations in differential diabatic cooling that result from local time differences over the grid array.

Solar Absorption. Computations were undertaken to describe the *relative* distribution of the total solar absorption in the atmosphere (including clouds) integrated over the half solar day, but for the sky conditions existing at the time of satellite passage. The time integration removed from the spatial variations the dependence of the absorption over each grid block on the local time. Neither ozone nor aerosol absorption was included in the computations, but these omissions do not significantly affect the relative distribution of the total absorption over the selected grid regions.

All computations of absorption were based on an empirical expression for the absorptivity α along atmospheric paths originating at the top of the atmosphere:

$$\alpha = \exp [-2.390 + 0.775 \log W - 0.978 (\log W)^2 - 0.222 (\log W)^3] \quad (2)$$

The form of the expression, in terms of the water-vapor path W , was taken from Korb et al. [9] and modified to accommodate those absorptivities presented by Yamamoto [19] for the high atmosphere. Although equation (2) may be applied directly for clear skies, the empirical approach was extended, with the aid of data from Korb and Möller [8], to include arbitrary sky conditions and a reflective lower boundary. Details of the method are described in an earlier report [6].

Within the sunlit day, the solar absorption rate varies differently with time for different sky conditions. Figure 4 illustrates estimated absorption rates during the half day for clear skies, a low cloud layer, a high cloud layer, and a combination of both layers—all for a single distribution of precipitable water in a summertime mid-latitude atmosphere. In general, the clouds increase the daily atmospheric absorption in comparison to clear skies, especially near noon. Low-based layers of water cloud are most effective in increasing the absorption. High clouds sometimes produce a smaller daily absorption than for clear skies, especially for short days (winter) with large solar zenith angles. Since the absorption rates are related to cloud type, they are also related to the albedo. If both the planetary albedo and the net insolation at the surface were known, it would be possible to specify directly the solar heating of the atmosphere. Unfortunately, instrumental problems and the sampling bias associated with the anisotropy of the reflected solar radiation have prevented the direct determination of reliable albedos from satellite measurements. Nevertheless, it is significant that solar heating *within* the atmosphere is usually larger for situations with high albedos than for low-albedo situations, whereas solar absorption by the earth or ocean is negatively correlated with the planetary albedo.

Latent and Boundary Heat Sources. At the time of

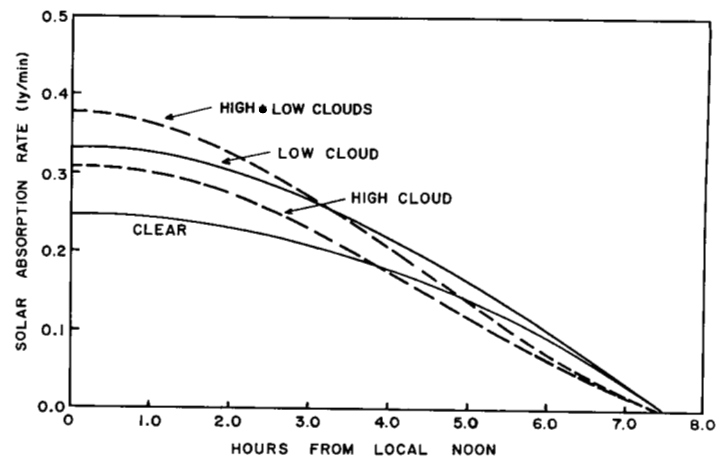


FIGURE 4.—Examples of estimated solar absorption rates in a summertime atmosphere for several sky-states.

satellite passage over the grid regions it was not possible to specify quantitatively the precipitation intensity or the excess of cloud generation over cloud dissipation. Since the areas with precipitation were almost entirely under radar surveillance, a qualitative classification of the release of latent heat was based on precipitation observations contained in the hourly summary charts of pertinent radar records and the available hourly surface reports. From the descriptions of no precipitation, some scattered occurrences of light precipitation, or extensive precipitation, each grid block was assigned the corresponding category (1) NONE, (2) SOME, or (3) EXTENSIVE, respectively. These categories provide some relative measure of the distribution of net condensation heating within the atmosphere. No satellite data were used in the description of precipitation distributions, but data from Channels 2 and 3 may assist in the descriptions of large-scale distributions of non-convective precipitation.

The net daily heat flux across the lower boundary commonly is a small residual between a nocturnal downward flux and an upward daytime flux. Without special measurements the surface heat flux is difficult to determine at any time. In summertime over land, with typical diurnal variations in the low-level temperature and wind structure, the stronger daytime mixing frequently leads to a net upward daily heat flux. The net daily flux is related to the energy available for transport at the surface and to the thermal advection over the boundary (land or water). In order to describe the relative spatial variations of the net surface heat flux that would result from upper-air conditions existing at analysis time, classifications of LOW, MEDIUM, and HIGH were assigned qualitatively on the basis of type of surface, cloudiness, and the presence or absence of low-level thermal advection. A LOW classification was assigned to grid blocks for which broken or overcast cloudiness and/or warm advection was present, or for which the lower boundary consisted of relatively cold water. The HIGH

classification was assigned to grid areas with pronounced cold-air advection and over dry land areas with clear skies. Other cases were classified as MEDIUM. Over grid blocks with a broken cirrus cover but with no lower clouds, the MEDIUM classification was used if the maximum-minimum temperature spread was not significantly suppressed. Although the classifications cannot describe the actual daily surface heat fluxes, they are believed to be meaningful in a relative sense.

Both the release of latent heat and the surface heat flux are closely related to atmospheric motions. It appears that these diabatic components might best be estimated from sufficiently sophisticated numerical models that include an objective treatment of cloudiness and water vapor.

6. RESULTS OF ANALYSES

A list of definitions of pertinent symbols is given in table 1. For the purpose of illustrating the degree of direct correspondence between variables within the orbital swaths, some linear correlation coefficients were computed. The coefficients are given in table 2, along with means and standard deviations. It is likely that some of the correlation coefficients would be increased if actual, rather than mean, surface temperatures were used in computations for each grid block. Satellite data have been averaged over each grid, but are otherwise unaltered from original listings.

As expected, a high linear correlation exists between the mean outgoing long-wave flux and the Channel 2 temperature. Even more significant is the fact that T_2 is better correlated with the divergence (cooling) of the total radiative flux, infrared and solar, than with the infrared flux divergence alone. Furthermore, the total radiational cooling is somewhat better related to T_2 than to the non-dimensional representations of the cloudiness for downward views, although only the total cloudiness N is included in table 2. The high negative correlation between T_2 and the available daytime measurements from

TABLE 1.—Definitions of symbols

Symbol	Definition
E	Potential plus internal energy per unit area in column from terrain surface to 100 mb. (joules/m. ²).
V	Precipitable water in entire atmospheric column (pr. cm.).
N	Amount of total cloud.
h	Average cloud top, given as average fraction of V below cloud top.
d	Average cloud depth, or "bulk", given as average fraction of V within cloud.
T_2	Average equivalent blackbody temperature, Channel 2 (°K.).
F_3	Average flux of reflected solar radiation, Channel 3 (watts/m. ²).
FL	Outgoing flux of long-wave radiation from earth-atmosphere (ozone excluded) (ly./min.).
DL	Long-wave flux divergence (cooling in the atmosphere) (ly./min.).
DR	Total radiational (long-wave and short-wave) flux divergence in the atmosphere (ly./min.).

Channel 3 indicates that much of the information in F_3 is also available from T_2 on the given grid scale.

A negative correlation of the total potential energy E with diabatic cooling (or positive correlation with diabatic heating) suggests a generation of available potential energy. In the four cases presented here only a slight negative correlation between E and the total radiative cooling persists. Since the cooling is related to T_2 , a similar correlation exists between E and T_2 . Variations in the terrain elevation have exerted an influence on the distribution of E ; the influence might have been segregated by grouping the data according to elevation.

The diabatic heat sources from the release of latent heat and from the surface heat flux were not specified quantitatively and were not included in the correlation analyses. However, for all grid blocks, relative estimates of both terms are presented in tables 3 and 4 in the form of frequency distributions. Since these distributions include data from all four passes, degradation in the response from Channel 2 between Passes 4 and 44 may have altered slightly the relationship to T_2 .

Table 3 displays the association between the estimated heating from condensation in the atmosphere and (a) E , (b) T_2 , and (c) DR . It is apparent that the latent heating

TABLE 2.—Selected statistics for data associated with TIROS III orbital passes. Symbols are defined in table 1.

Pass 3 (18 grid blocks)							Pass 29 (16 grid blocks)						
Symbol	Correlation Coefficients				Mean	Standard Deviation	Symbol	Correlation Coefficients			Mean	Standard Deviation	
	E	N	T_2	F_3				E	N	T_2			
F_L -----	-0.45	-0.91	0.94	-0.92	0.358	0.051	F_L -----	-0.12	-0.87	0.96	0.336	0.036	
D_L -----	-.25	-.01	.46	-.21	.244	.026	D_L -----	.27	-.43	.72	.258	.023	
D_R -----	-.45	-.48	.81	-.62	.135	.028	D_R -----	-.12	-.59	.80	.139	.026	
E -----		.32	-.57	.51	205.0	9.7	E -----		.23	-.06	220.4	6.0	
N -----			-.81	.88	.490	.315	N -----			-.88	.584	.210	
T_2 -----				-.90	268.7	11.3	T_2 -----				263.3	9.8	

Pass 4 (42 grid blocks)							Pass 44 (24 grid blocks)						
Symbol	Correlation Coefficients				Mean	Standard Deviation	Symbol	Correlation Coefficients			Mean	Standard Deviation	
	E	N	T_2	F_3				E	N	T_2			
F_L -----	-0.45	-0.93	0.94	-0.91	0.363	0.048	F_L -----	-0.57	-0.89	0.96	0.385	0.049	
D_L -----	.34	.17	.10	-.09	.255	.022	D_L -----	.40	.53	-.02	.254	.033	
D_R -----	-.22	-.50	.69	-.59	.141	.023	D_R -----	-.02	-.02	.50	.145	.023	
E -----		.48	-.42	.45	211.2	12.8	E -----		.67	-.57	203.6	14.0	
N -----			-.89	.92	.438	.317	N -----			-.82	.348	.326	
T_2 -----				-.89	271.9	11.7	T_2 -----				268.0	8.8	

TABLE 3.—Frequency distributions of estimated heating from condensation (L)

(a) Total potential energy E (joules/m. ²)				
L	≤ 200	201-213	214-220	≥ 221
NONE.....	21	12	6	6
SOME.....	5	13	11	6
EXTENSIVE.....	0	2	6	12

(b) Channel 2 temperature T_2 (°K.)				
L	≤ 260	261-268	269-275	≥ 276
NONE.....	1	4	19	21
SOME.....	11	9	10	5
EXTENSIVE.....	12	6	1	1

(c) Total radiative flux divergence D_R (ly./min.)				
L	≤ 0.125	0.126-0.133	0.145-0.195	≥ 0.160
NONE.....	3	9	16	17
SOME.....	10	10	9	6
EXTENSIVE.....	12	5	2	1

is positively correlated with the total potential energy, thereby suggesting a generation of potential energy just as did the total radiational cooling. Furthermore, there is a negative correlation to T_2 and D_R (positive correlation in terms of latent cooling). It appears likely that the Channel 2 temperature is fairly well correlated to the average diabatic cooling expressed by infrared cooling, solar heating, and the latent heating.

Table 4 displays the relationship between the estimated relative surface heat flux to the atmosphere and (a) E , (b) T_2 , and (c) the estimated rate of release of latent heat. For the conditions prescribed over the grid blocks, the estimated average surface heat flux acts in opposition to the other diabatic terms in that it promotes a destruction of eddy potential energy and is correlated posi-

TABLE 4.—Frequency distributions of estimated surface heat flux (S)

(a) Total potential energy E (joules/m. ²)				
S	≤ 200	201-213	214-220	≥ 221
LOW.....	0	7	15	15
MEDIUM.....	4	15	8	8
HIGH.....	22	5	0	1

(b) Channel 2 temperature T_2 (°K.)				
S	≤ 260	261-268	269-275	≥ 276
LOW.....	17	11	6	3
MEDIUM.....	7	8	16	4
HIGH.....	0	0	8	20

(c) Release of latent heat L			
S	None	Some	Extensive
LOW.....	8	12	17
MEDIUM.....	13	19	3
HIGH.....	24	4	0

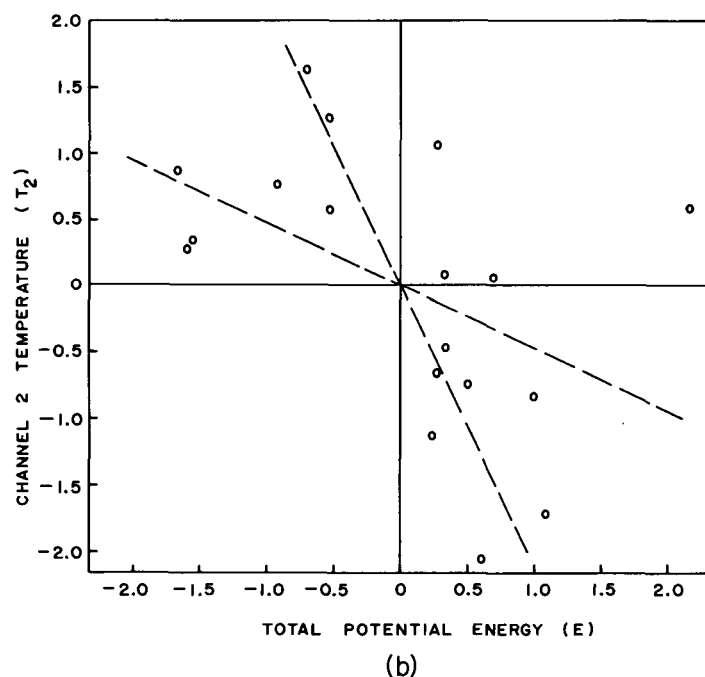
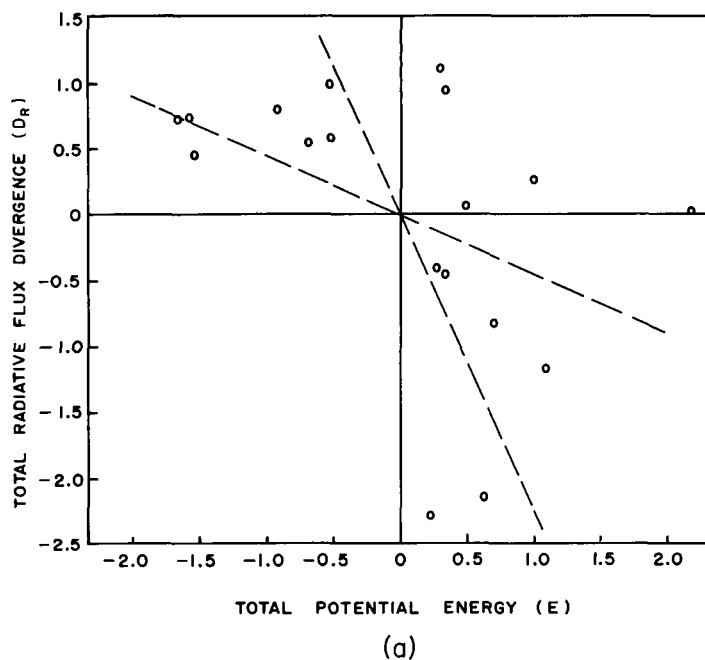


FIGURE 5.—Scatter diagrams for selected variables from 4-by-4-deg. grids along pass 3. Each point represents departure from mean divided by standard deviation. Regression lines indicated.

tively with the Channel 2 temperature (for other terms T_2 is correlated positively with relative diabatic cooling). Although the net surface heat flux is probably the smallest diabatic term on the scale considered here, it could be more significant at larger scales or at other localities. Table 4(c) shows the expected negative correlation with the latent heating. The latter relationship is not always simple; for example, cold-air advection may induce a large surface heat flux and initiate significant convective showers at the same time.

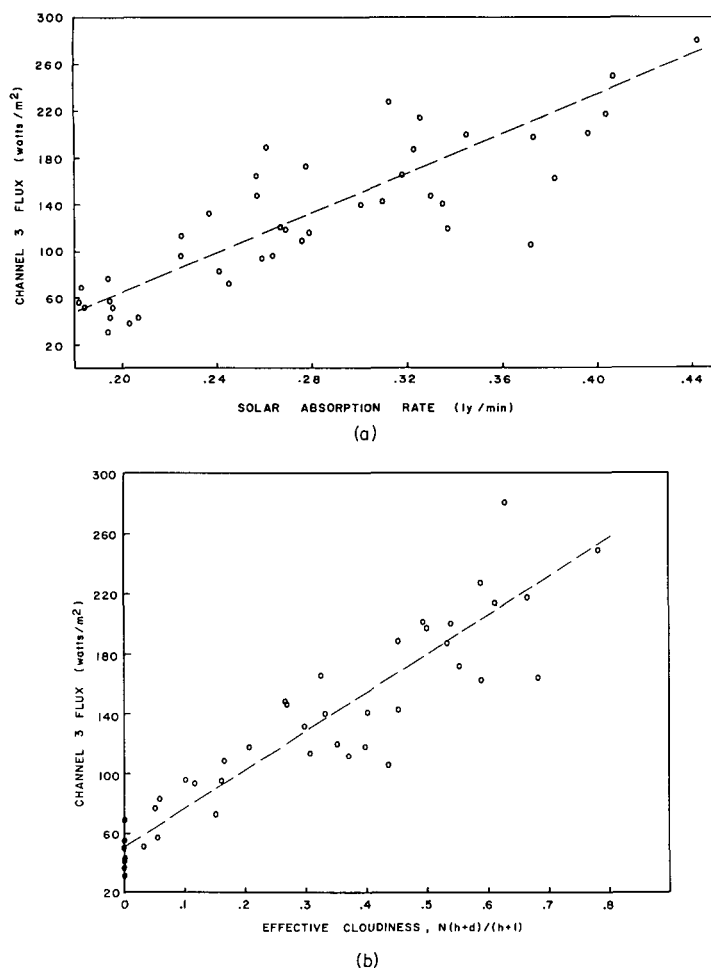


FIGURE 6.—Channel 3 flux for 4-by-4-deg. grids along pass 4 versus computed solar absorption rate and a parameter describing the effective cloudiness (symbols defined in table 1). Dashed lines suggest linear fit.

In order to illustrate further some of the relationships contained in the data, sample scatter diagrams are presented for several variables during each orbital pass. With data from 18 grid blocks along Pass 3, figure 5 shows the relationship (a) between the total radiative flux divergence and the total potential energy and (b) between the Channel 2 temperature and the total potential energy. In both cases each variable has been standardized into the ratio of the departure from the mean to the standard deviation. Although there may be little or no correlation for any given case, the slight correlation of heating to total potential energy that is evident in figure 5 is described just as well by the unaltered Channel 2 temperatures as by the computed radiative flux divergence.

By an examination of the correlation between the total potential energy and the vertical motions over the same grid, some clues were sought about the possible conversion of eddy potential into eddy kinetic energy. Vertical motions in the troposphere were computed (see Appendix) for the grid blocks corresponding to Passes 3 and 4. Partly as a result of the inherent inaccuracies of vertical motion computations, especially for vertical motions of

small magnitudes, no truly significant correlations were found. Although centers of significant vertical motion in the mid-troposphere could have played an important role in triggering a build-up or dissipation of eddy kinetic energy locally, no pronounced net energy conversion was apparent over the selected grid region on the given day.

Figure 6 compares the observed Channel 3 flux during Pass 4 with (a) the computed solar absorption rate in the atmosphere (ozone excluded) for the time of satellite passage, and (b) a non-dimensional parameter that depicts the proximity and bulk of the average cloud cover in view. The first illustration indicates that the observed flux is generally related to the coincident solar absorption rates (which depend on solar zenith angle) for the atmosphere, clouds included. Therefore, both the cloud reflectance and the total absorption within the atmosphere lead to a Channel 3 flux that is inversely related to the solar energy available for heating land and ocean.

Some satellite information relating to the bulk or downward extent of the average cloudiness should aid any assessment of the atmospheric heat budget. In this study the non-dimensional parameters h and d (see table 1) describe the average cloud-top height and the average cloud bulk, respectively, of the cloudiness within each grid block. Neither parameter explicitly indicates geometrical distance. A non-dimensional cloudiness parameter, C , for downward views was defined for each grid block as

$$C = N \frac{h+d}{h+1} \quad (3)$$

where N is the total cloud amount. The parameter C , which varies between the limits of 0 and 1, was designed to provide a non-zero statistic for those high clouds for which d had been set equal to zero. Figure 6b shows that F_3 relates quite well to C , and it follows that if the total cloud amount N and the average top-height h were known, some measure of d could be deduced. Photographs provide a good estimate of N , whereas T_2 is correlated with $N \cdot h$ (cf. fig. 2), but uncertainties in the cloud specifications persist in all suggested relationships.

In addition to information on the high-altitude radiation balance obtainable from satellite measurements, information is needed on the radiation balance of the lower boundary of the atmosphere. Figure 7a illustrates the distributions of the Channel 2 temperatures and the computed average net long-wave radiation at the lower boundary of grid blocks along Pass 29. In view of the differences between cloud tops and cloud bases, as well as the inadequacies of the nephanalysis, the scatter is not surprising. However, from figure 7b it is apparent that the cloudiness parameter C shows a better relationship than T_2 to the net long-wave radiation at the surface.

With the data from Pass 44, figure 8a illustrates the relationship between T_2 and the computed outgoing long-wave flux for the mean surface temperature. In the western portion of the swath the terrain was viewed under

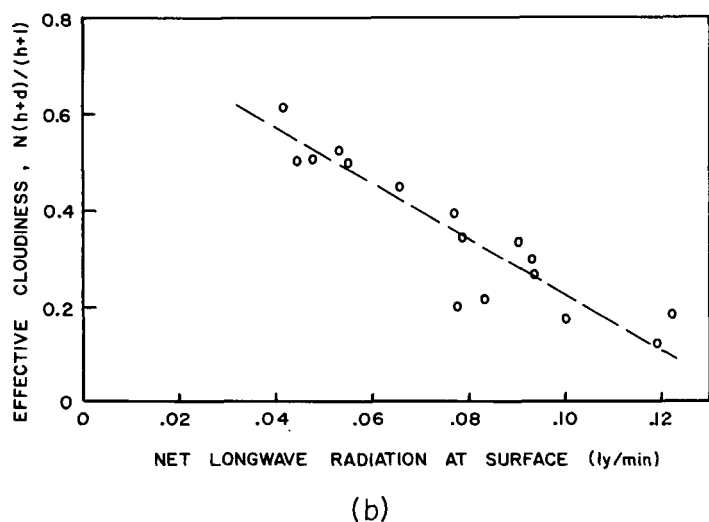
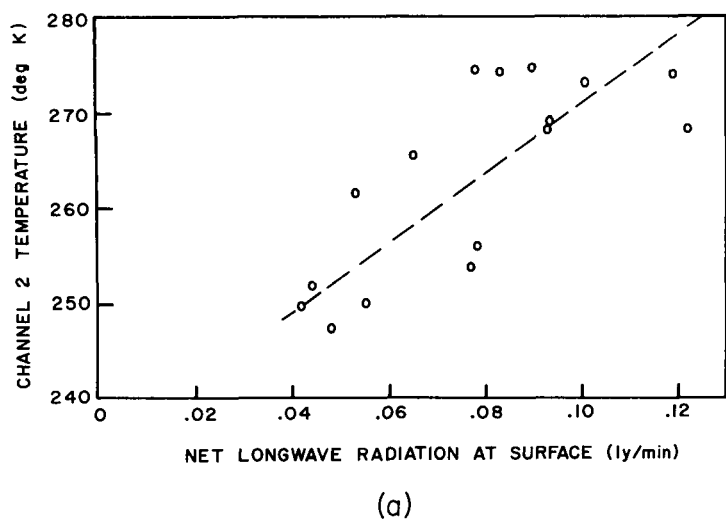


FIGURE 7.—Computed net long-wave radiation at surface of 4-by-4-deg. grids along pass 29 versus Channel 2 temperature and a parameter describing the effective cloudiness (symbols defined in table 1). Dashed lines suggest linear fit.

clear skies near the time of minimum surface temperature. Therefore, a sizable alteration in the relationship might be anticipated when the mean surface temperatures (averages for the half-day) are replaced by the surface temperatures observed at the time of satellite passage. Figure 8b shows that the resulting change is small and occurs only for the largest values of outgoing flux (clear skies), but the relationship remains linear. The reduction of the maximum fluxes results from the lower surface temperatures. When the variations in nadir angle are taken into account, the outgoing flux derived from T_2 in the manner suggested by Wark et al. [18] differs from that described by figure 8b, especially at high temperatures. The difference probably is due to instrumental degradation and, in part, to the fact that no climatological smoothing has been introduced in the present application.

Figure 8c illustrates the relationship between the effec-

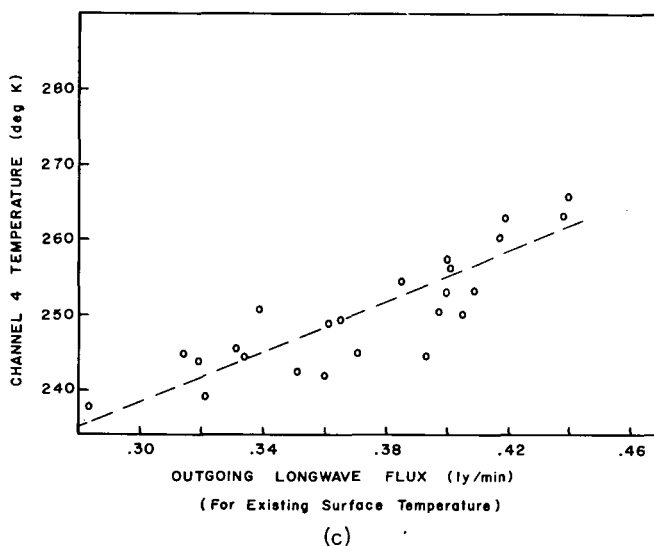
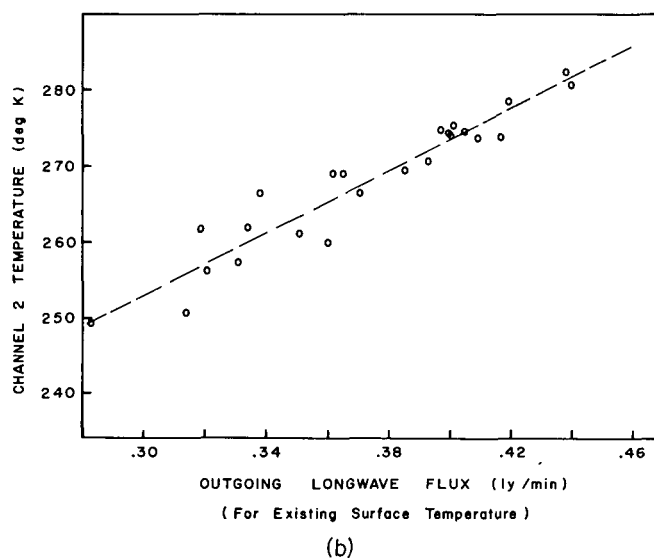
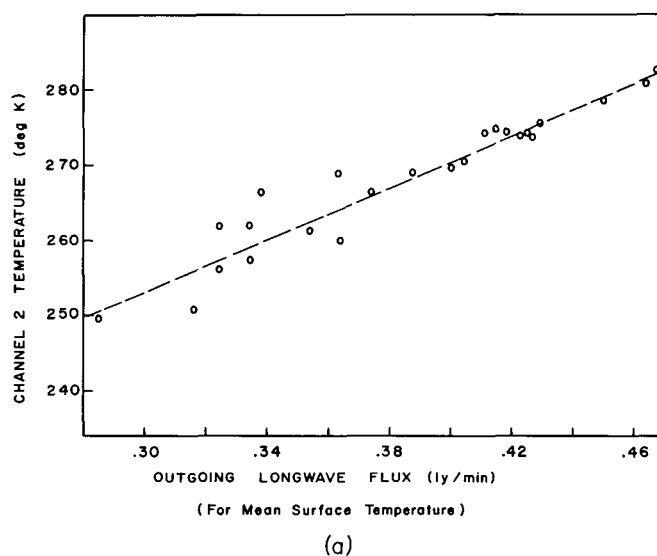


FIGURE 8.—Computed outgoing long-wave flux for 4-by-4-deg. grids along pass 44 versus Channel 2 and Channel 4 temperatures. Dashed lines suggest linear fit.

tive temperature from the broad Channel 4 and the corresponding computed outgoing flux as in figure 8b. There appears to be more scatter than with the Channel 2 temperature, and the non-linearity of the relationship is probably due to the increased limb darkening for Channel 4; the nadir angles for the smaller fluxes averaged almost 13 deg. larger than the nadir angles for the largest fluxes during this portion of Pass 44. With a proper restriction on the largest nadir angle allowed, the smaller limb darkening for Channel 2 means that Channel 2 is better suited for direct application than is Channel 4.

7. SUMMARY

Analyses of TIROS III radiation data from four orbital sections were confined primarily to Channel 2 and Channel 3 (daytime only) because these channels contained most of the useful information. Conventional meteorological data that were obtained concurrently with the satellite data were analyzed in order to provide a basis for determining the applicability of the satellite measurements to specifications of the diabatic heating and cooling within the atmosphere on a 4-by-4-deg. grid scale.

Results show that variations of the Channel 2 temperature are well related to variations in the outgoing long-wave flux and, to a lesser extent, to the effective cloudiness. Because of its responsiveness to changes in earth-atmosphere emittance and its smaller limb darkening, the Channel 2 temperature is more useful for direct application than the Channel 4 temperature. The relationship between the Channel 2 temperature and the total radiative flux divergence (long-wave and short-wave) is better than the relationship between Channel 2 and the long-wave flux divergence. The Channel 2 temperature is correlated in the same sense to the latent heating component as it is to the radiative diabatic component, but is related in the opposite sense to the boundary heat flux. It appears that the effective temperature of Channel 2 in its tabulated form may be related to the total diabatic cooling within the atmosphere; objective cloud information and other radiometric observations may assist in the establishment of quantitative relationships. The tabulated Channel 3 fluxes show a relationship to the solar absorption rates and to a non-dimensional cloud parameter that describes the amount, height, and bulk of the average cloudiness.

The distributions of both the total radiative flux divergence and the released latent heat suggested some generation of eddy potential energy for the 4-by-4-deg. grid scale, whereas the distribution of the boundary heat flux suggested the destruction of eddy potential energy. Since the differential boundary heat flux probably produced the smallest diabatic effect, a small net generation for these July cases was suggested. The correlation between the total potential energy and the Channel 2 temperature was indicative of this generation.

Further empirical studies are needed for different

climatic regions and seasons in order to establish the feasibility of specifying the distribution of atmospheric diabatic heating from satellite measurements and numerical computations. Ultimately, it should be possible to obtain directly a useful satellite measure of the spatial and temporal distributions of the mean atmospheric temperature or thickness—and the variations of potential energy.

APPENDIX

The average vertical motion ω_p at a surface of constant pressure P can be computed from actual average wind components measured at a number of heights above a lower boundary of any configuration. If the spatially-varying surface pressure is p_0 , then, for a grid block bounded by geographical latitudes and longitudes,

$$\widehat{\omega_p} = \frac{\widehat{\partial p_0}}{\partial t} + [R(\sin \varphi_N - \sin \varphi_S)]^{-1} \left\{ \frac{(\varphi_N - \varphi_S)}{(\lambda_E - \lambda_W)} [(\overline{u\delta_p})_E - (\overline{u\delta_p})_W] + (\overline{v\delta_p})_N \cos \varphi_N - (\overline{v\delta_p})_S \cos \varphi_S \right\}$$

where R =earth's radius, φ =latitude, λ =longitude, u =zonal wind component, v =meridional wind component, $\delta_p = p_0 - P$, and the subscripts E, W, N, S identify the lateral grid boundaries by direction. For an extension through a higher layer, the factorable pressure increment between constant-pressure levels would replace the spatially-varying δ_p and the computed $\widehat{\omega_p}$ at the base of the layer would replace the observed $\widehat{\partial p_0 / \partial t}$.

Averaging symbols are defined below:

$$\overline{(\quad)} = (p_2 - p_1)^{-1} \int_{p_1}^{p_2} (\quad) dp;$$

$$\widehat{(\quad)} = \iint (\quad) \cos \varphi d\lambda d\varphi / \iint \cos \varphi d\lambda d\varphi, \text{ over the grid areas;}$$

$$\widetilde{(\quad)}_m = (\varphi_N - \varphi_S)^{-1} \int_{\varphi_S}^{\varphi_N} (\quad)_m d\varphi, \text{ where } m = E \text{ or } W,$$

$$\widetilde{(\quad)}_n = (\lambda_E - \lambda_W)^{-1} \int_{\lambda_W}^{\lambda_E} (\quad)_n d\lambda, \text{ where } n = N \text{ or } S.$$

ACKNOWLEDGMENTS

The author gratefully acknowledges the participation and assistance from personnel of the Aerophysics Laboratory of Stanford Research Institute, especially from Mr. William Viezee, Mr. Robert L. Mancuso, Mr. John D. Weaver, and Mr. James R. Moeller.

REFERENCES

1. W. R. Bandeen, R. E. Samuelson, and I. Strange, "TIROS III Radiation Data User's Manual Supplement," Goddard Space Flight Center, Dec. 1963, 56 pp.
2. J. A. Brown, Jr., "A Diagnostic Study of Tropospheric Diabatic

- Heating and the Generation of Available Potential Energy," *Tellus* vol. 16, No. 3, Aug. 1964, pp. 371-388.
3. P. F. Clapp, "Comments on 'Analysis of Satellite Infrared Radiation Measurements on a Synoptic Scale' and 'Synoptic Use of Radiation Measurements from Satellite TIROS II'," *Monthly Weather Review*, vol. 90, No. 7, July 1962, pp. 287-288.
 4. P. F. Clapp and F. J. Winninghoff, "Tropospheric Heat Sources and Sinks at Washington, D.C., Summer 1961, Related to the Physical Features and Energy Budget of the Circulation," *Monthly Weather Review*, vol. 91, Nos. 10-12, Oct.-Dec. 1963, pp. 494-504.
 5. P. A. Davis, "The Application of Infrared Flux Models to Atmospheric Data," *Journal of Applied Meteorology*, vol. 4, No. 2, Apr. 1965, pp. 263-271.
 6. P. A. Davis, "Satellite Radiation Measurements and the Atmospheric Heat Balance," Final Report, contract NAS 5-2919, Stanford Research Institute, Menlo Park, Calif., July 1964.
 7. P. A. Davis and W. Viezee, "A Model for Computing Infrared Transmission through Atmospheric Water Vapor and Carbon Dioxide," *Journal of Geophysical Research*, vol. 69, No. 18, Sept. 15, 1964, pp. 3785-3794.
 8. G. Korb and F. Möller, "Theoretical Investigation on Energy Gain by Absorption of Solar Radiation in Clouds," Final Report, contract DA91-591-EUC-1612, Ludwig-Maximilians Universität, Meteorologisches Institut, Munich, 1962, 185 pp.
 9. G. Korb, J. Michalowsky, and F. Möller, "Investigations on the Heat Balance of the Troposphere," Technical Report No. 1, contract AF61(514)-863, Johannes-Gutenberg Universität, Meteorologisch-Geophysikalisches Institut, Mainz, Aug. 1956, 94 pp.
 10. A. F. Krueger, J. S. Winston, and D. A. Haines, "Computations of Atmospheric Energy and Its Transformation for the Northern Hemisphere for a Recent Five-Year Period," *Monthly Weather Review*, vol. 93, No. 4, Apr. 1965, pp. 227-238.
 11. E. N. Lorenz, "Available Potential Energy and the Maintenance of the General Circulation," *Tellus*, vol. 7, No. 2, May 1955, pp. 157-167.
 12. Y. Mintz, "Meteorological Satellites and Numerical Weather Prediction," Symposium on the Application of Passive Microwave Technology to Satellite Meteorology, Memorandum RM-3401-NASA, The Rand Corp., Aug. 1963, pp. 241-253.
 13. A. H. Oort, "On Estimates of the Atmospheric Energy Cycle," *Monthly Weather Review*, vol. 92, No. 11, Nov. 1964, pp. 483-493.
 14. R. R. Sabatini and V. E. Suomi, "On the Possibility of Atmospheric Infrared Cooling Estimates from Satellite Observations," *Journal of the Atmospheric Sciences*, vol. 19, No. 4, July 1962, pp. 349-350.
 15. Staff, Aeronomy and Meteorology Division, NASA Goddard Space Flight Center, "TIROS III Radiation Data User's Manual," Goddard Space Flight Center, Aug. 1963, 71 pp.
 16. Staff, Aeronomy and Meteorology Division, NASA Goddard Space Flight Center, and Meteorological Satellite Laboratory, U.S. Weather Bureau, "TIROS III Radiation Data Catalog," Goddard Space Flight Center, Dec. 1962, 388 pp.
 17. V. E. Suomi and W. C. Shen, "Horizontal Variation of Infrared Cooling and the Generation of Eddy Available Potential Energy," *Journal of the Atmospheric Sciences*, vol. 20, No. 1, Jan. 1963, pp. 62-65.
 18. D. Wark, G. Yamamoto, and J. Lienesch, "Methods of Estimating Infrared Flux and Surface Temperature from Meteorological Satellites," *Journal of the Atmospheric Sciences*, vol. 19, No. 5, Sept. 1962, pp. 369-384.
 19. G. Yamamoto, "Direct Absorption of Solar Radiation by Atmospheric Water Vapor, Carbon Dioxide, and Molecular Oxygen," *Journal of the Atmospheric Sciences*, vol. 19, No. 2, Mar. 1962, pp. 182-188.

[Received April 27, 1965; revised July 12, 1965]